

## 4 SAR and SAR Interferometry

### 4.1 Synthetic Aperture Radar

Imaging radar provides a two-dimensional representation of the radar reflectivity of a scene [174]. In general, a monostatic radar system consists of a pulsed microwave transmitter, an antenna which can be used for transmission and reception, and a receiver. It is mounted on a moving platform such as an airplane or satellite, and the antenna beam is pointed slant-wise towards the ground, orthogonal to the flight direction, and the antenna is referred to as range or across-track direction. The transmitter pulse is radiated by the antenna, backscattered from the terrain and sensed by the receiver. The platform motion provides the scanning in direction of the sensor trajectory which is referred to as azimuth or along-track direction.

The signal time delay is proportional to the scatterer range. Scatterers at different distances are resolved because of the different time delays of their echos. Consequently the resolution in range direction depends on the effective transmitted pulse length  $\tau$  or alternatively on the signal bandwidth  $W$

$$\rho_{rg} = \frac{c\tau}{2} = \frac{c}{2W} \quad (4.1)$$

where  $c$  is the propagation velocity of EM radiation. As an example, a radar with a bandwidth of 100 MHz provides a theoretical range resolution of about 1.5 m. Technological limitations in the radar hardware make the generation of very short pulses with sufficient high energy, required to obtain a backscattered echo with adequate energy, difficult. Radar systems overcome this limitations by transmitting a linear frequency modulated pulse, known as chirp, with a time-bandwidth product significantly greater than one. This provides the large bandwidth which is necessary for achieving the required resolution, by spreading the energy over a long pulse duration. After reception, the received signal can be compressed into a pulse with a time-bandwidth product approximately equal to unity by applying the concept of matched filtering [175], [176].

In the azimuth direction, the resolution depends on the angular resolution of the antenna beam  $\alpha$ , that is inversely proportional to its physical size in the azimuth direction  $D$

$$\alpha \simeq \frac{\lambda}{D} \quad (4.2)$$

$\lambda$  is the radiation wavelength. The spatial azimuth resolution  $\rho_{az}$  at a fixed range  $R$  is then given by the product of the angular resolution  $\alpha$  and the range  $R$

$$\rho_{az} = \alpha R \simeq \frac{\lambda}{D} R \quad (4.3)$$

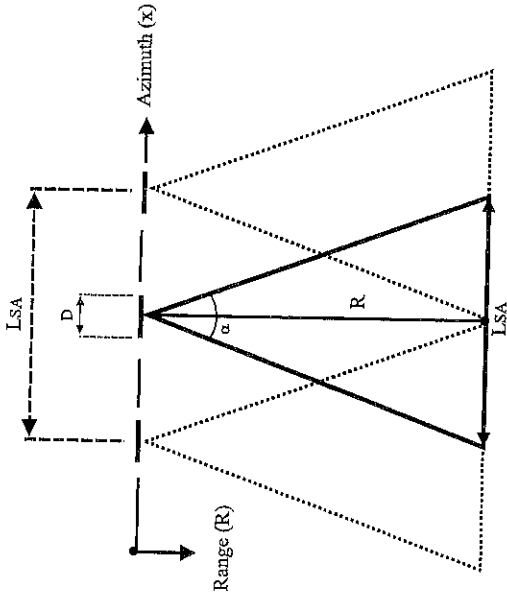


Figure 4.1: SAR imaging geometry.

Obviously, a constant angular resolution provides an azimuth resolution that decreases with radial distance. Especially at long ranges high resolution in azimuth becomes difficult because of the need of unreasonably large antennas.

A Synthetic Aperture Radar (SAR) achieves, even with a short antenna, high spatial resolution in azimuth by using the concept of "synthetic aperture": The appropriate coherent integration of the signals received from a scatterer by an array of antenna elements is used in order to synthesise a large antenna with a very narrow beam. In the case of SAR, there are no distinct antenna elements; as the radar sensor is in motion, the same antenna is used to measure the backscattered signal in different positions building up sequentially a synthetic aperture (see Figure 4.1). If the scatterers are stationary, the received echoes can be considered to be obtained through an array of antenna elements. Similar as in the case of a real aperture, the angular resolution of the synthetic aperture is given by

$$\alpha_{SA} \simeq \frac{\lambda}{2L_{SA}} \quad (4.4)$$

where  $L_{SA}$  denotes the length of the synthetic aperture. The factor 2 accounts for the effect of sequential emission of the elements of the synthesised antenna in the case of SAR: The phase difference between equally spaced elements of the synthetic aperture is over the two-way-path difference, and thus it is twice that of a conventional real antenna where the elements transmit simultaneously. The maximum length of the effective synthetic aperture is given by the time that the scatterer is illuminated by the radar beam, and it equals the width on the ground

illuminated by the real antenna

$$L_{SA} = \alpha R = \frac{\lambda}{D} R \quad (4.5)$$

Note, that the synthetic aperture length is proportional to range and inversely proportional to the physical antenna size. The angular resolution of the synthetic aperture is then given by

$$\alpha_{SA} = \frac{D}{2R} \quad (4.6)$$

Because of the range-dependent aperture length, the angular resolution of the synthetic aperture is no more constant but improves with increasing range. The maximally achievable spatial resolution in azimuth at a range  $R$  results as

$$\rho_{az} = \alpha_{SA} R = \frac{D}{2} \quad (4.7)$$

According Eq.(4.7), the spatial resolution of the synthetic aperture is independent of the range distance and the wavelength and depends only on the dimension of the real antenna. Exactly this crucial fact makes possible the operation of high resolution SAR systems not only on airborne but also on spaceborne platforms. Detailed descriptions of the theoretical aspects of SAR systems can be found among others in [177],[178],[179],[180].

## 4.2 Point Scatterer Response

To review the process of SAR data acquisition and image formation, it is convenient to consider the case of a single point-scatterer illuminated by a radar sensor moving at a constant height with a constant velocity  $\vec{v}$  along a straight trajectory in  $x$ -direction. The point-scatterer can be described in the two-dimensional azimuth/range  $(x, R)$  space as a Dirac delta function  $\delta(x - x_0, R - R_0)$  at azimuth coordinate  $x_0$  and the range distance at the point of closest approach  $R_0$ . In the following the azimuth/range space  $(x, R)$  will be referred as the object space while the azimuth/range-time space  $(x, t)$  as the data space.

The pulse transmitted by the radar sensor, at a carrier frequency  $\omega_0$  with an envelope  $p(t)$  like a rect-function, and a bandwidth  $\omega_w$ , can be expressed as

$$s_t(t) = p(t) \exp(i\omega t) \quad (4.8)$$

The signal frequency  $\omega$  varies from  $\omega_0 - \omega_w/2$  to  $\omega_0 + \omega_w/2$ . The received echos from the scatterer are delayed replicas of the transmitted signal. The fact that the transmitted pulses travel with a velocity much greater than the platform velocity, permit us to neglect the effect of sensor motion during the travelling time of the pulse. Thus, the received echos can be written as

$$s_r(t; R_0) = p(t - 2R(x, R_0)/c) \exp i(\omega t - \omega_0 2R(x, R_0)/c) \quad (4.9)$$

where  $R(x; R_0)$  is the sensor-scatterer distance. After coherent quadratic demodulation [180]<sub>1</sub>[179], the carrier frequency is removed, and the received signal becomes

$$s_r(t; R_0) = p(t - 2R(x; R_0)/c) \exp(-i\omega_0 2R(x; R_0)/c) \quad (4.10)$$

The phase of the received echo is a function of the sensor position along its trajectory, depending on the variation of the sensor-scatterer distance which is known as the range history

$$R(x; R_0) = \sqrt{R_0^2 + x^2} = R_0 \sqrt{1 + \frac{x^2}{R_0^2}} \simeq R_0 \left(1 + \frac{1}{2} \frac{x^2}{R_0^2}\right) = R_0 + \frac{1}{2} \frac{x^2}{R_0} \quad (4.11)$$

From Eq.(4.11) follows that the echos received from the point scatterer are not positioned at the same range time  $t_0 = 2R_0/c$  but lie in the data space on a hyperbolic curve with apex in  $\#0$ . The curvature of the curve changes for different range distances  $R_0$ . The information about amplitude, phase, and location of the point scatterer is dispersed along this hyperbolic curve, which can be approximated by a parabolic form according Eq.(4.11).

After range compression, the pulse envelope  $p(t)$  can be approximated by a  $\delta$ -function, and the ensemble of all echos received from the scatterer can be written as

$$h(x; t; R_0) = \delta(t - 2R(x; R_0)/c) \exp(-i\omega_0 2R(x; R_0)/c) \quad (4.12)$$

Figure 4.2 shows on the left a simulated response as it will be acquired by a SAR system from an idealised point scatterer; and in the middle, the point scatterer response  $h(x; t; R_0)$  after range compression.

Recapitulating, the process of data acquisition can be described as a transformation of the point-scatterer  $\delta(x - x_0, R - R_0)$  from the object space into the point-scatterer response  $h(x; t; R_0)$  in the data space where, in consequence of Eq.(4.11), range-time  $t$  and range  $R$  are not interchangeable. The exponential term of Eq.(4.12) expresses the range history in terms of a phase history of the received signal. It is called azimuth chirp since - under the parabolic approximation - the phase becomes quadratic corresponding to a linear frequency modulation

$$\phi(x) = 2\omega_0 R(x; R_0)/c \simeq \frac{2\omega_0}{c} \left(R_0 + \frac{1}{2} \frac{x^2}{R_0}\right) \quad (4.13)$$

The first phase term is a constant, and it is proportional to the closest approach range  $R_0$ . It is the key factor in SAR interferometry, but for the SAR image formation it can be ignored. On the contrary, the azimuth varying second phase term is essential in SAR image processing, because it allows the compression of the received signal in the azimuthal direction. It is convenient to decompose the two phase terms introducing a normalised sensor-scatterer distance variation  $\Delta r(x; R)$ , defined as the difference between the actual range  $R(x; R_0)$  and  $R_0$ ,

$$\Delta R(x; R_0) = R(x; R_0) - R_0 = \sqrt{R_0^2 + x^2} - R_0 \simeq \frac{1}{2} \frac{x^2}{R_0} \quad (4.14)$$

$\Delta R(x; R_0)$  expresses the deviation of the point-scatterer response from a straight line at  $R_0$  and is referred in the literature as range migration. Using  $\Delta R(x; R_0)$  instead of  $R(x; R_0)$  in

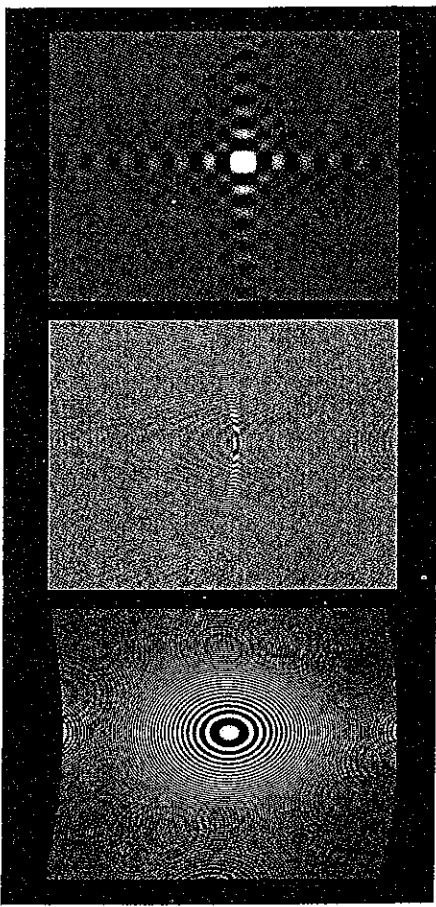


Figure 4.2: Point scatterer response. Left: before range compression. Middle: after range compression. Right: after range migration correction and azimuth compression.

Eq.(4.12) we obtain a normalised point scatterer response with apex shifted now at the origin of the  $(x, t)$ -coordinate system.

$$h(x, t; R_0) = \delta(t - 2\Delta R(x; R_0)/c) \exp(-i\omega_0 2\Delta R(x; R_0)/c) \quad (4.15)$$

$h(x, t; R_0)$  is a function of azimuth  $x$ , range time  $t$  and depends on the scatterer range  $R_0$ . The range migration  $\Delta R(x; R_0)$  introduces a coupling between range and azimuth coordinates making the problem of SAR image processing intrinsically a two-dimensional and non-separable problem.

### 4.3 SAR Data Processing

The objective of SAR processing is to transform the raw data acquired by the SAR system into a two-dimensional high resolution image. In the context of the point-scatterer concept this means the transformation of the dispersed point scatterer response from the data space into a narrow point spread function in the object image space in order to reconstruct the original point-scatterer  $\delta(x - x_0, R - R_0)$ . The commonly adopted approach is based on the concept of matched filtering: The image  $i(x, R)$  is obtained by the two-dimensional range variant correlation in azimuthal direction of the acquired raw data  $d(x, t)$  with the normalised point-scatterer response  $h(x, t)$

$$i(x, R) = \iint d(\xi, t) h^*(\xi - x, t - 2R(x; R_0)/c) d\xi dt = \int d(x, t) \odot_x h^*(x, t - 2R(x; R_0)/c) dt \quad (4.16)$$

where  $\odot_x$  denotes the correlation in the azimuth  $x$ -direction. Eq.(4.16) is known as the focusing equation, and it states the most direct method of image formation: An image point is obtained

by selecting the raw data along the range migration trajectory, correcting their phases according to the azimuth chirp phase function, and adding them up. However, the time domain correlation as given in Eq.(4.16) is, because of the large number of samples, very time consuming and it is not used in practice for high resolution systems.

In cases where range migration can be neglected,  $h^*(x, t; R) \mapsto h^*(x)$ , and the compression becomes decoupled in azimuth and range. Then focusing equation of Eq.(4.16) reduces to a set of one-dimensional correlations. On the other hand, if only a narrow range segment around  $r = R_0$  is to be focused, the variance of the range migration trajectory can be neglected, and  $h^*(x, t; R) \mapsto h^*(x, t; R_0)$ . In this case, Eq.(4.16) can be replaced by a two-dimensional space invariant correlation

$$i(x, R = ct/2) \simeq d(x, t) \odot_x \odot_t h^*(x, t; R_0) \quad (4.17)$$

Using the fact that a correlation can be expressed as a convolution with a time/space inverted correlation kernel and by applying the *Convolution Theorem* [181],[182], Eq.(4.17) can be transformed in the two-dimensional frequency domain as

$$I(\kappa_x, \kappa_R = 2\omega/c) = D(\kappa_x, \omega) H^*(\kappa_x, \omega; R_0) \quad (4.18)$$

where  $I(\kappa_x, \kappa_R)$ ,  $D(\kappa_x, \omega)$ , and  $H(\kappa_x, \omega)$  are the two-dimensional Fourier transformations of  $i(x, R)$ ,  $d(x, t)$ , and  $h(x, t)$ , respectively. The wavenumbers  $\kappa_x$  and  $\kappa_R$  represent spatial angular frequencies in the  $x$ - and  $R$ -direction, and  $\omega$  is the angular frequency.  $H^*(\kappa_x, \omega; R_0)$  is the optimum transfer function for focusing a point-scatterer at a constant range  $R = R_0$ ; and it can be derived by the two-dimensional Fourier transformation of the point-scatterer response  $h(x, t; R_0)$  of Eq.(4.15)

$$\begin{aligned} H(\kappa_x, \omega; R_0) &= \iint h(x, t; R_0) \exp(-i(\kappa_x x + \omega t)) dx dt \\ &= \iint \delta(t - 2R(x; R_0)/c) \exp(-i\omega_0 2\Delta R(x; R_0)/c) \exp(-i(\kappa_x x + \omega t)) dx dt \end{aligned} \quad (4.19)$$

Using the Fourier transformation of the  $\delta$  function

$$\int \delta(t - t_0) \exp(-i\omega t) dt = \exp(-i\omega t_0) \quad (4.20)$$

the integral along the range time  $t$ -direction becomes

$$H(\kappa_x, \omega; R_0) = \int \exp(-i\Phi(x)) dx = \int \exp\left[-2i(\omega + \omega_0)\Delta R(x; R_0)/c\right] \exp(-i\kappa_x x) dx \quad (4.21)$$

An accurate approximation of this integral can be found using the stationary phase approximation. Heuristically the approximation of stationary phase takes advantage of the fact that the integrand is oscillating by many cycles over the interval of integration. Thus, the contributions to the integral over most of the  $x$ -interval tend to cancel out each other with exception of the stationary points  $x_*$ , at which the derivative of the phase of the integrand is zero

$$\frac{d}{dx} \exp(-i\Phi(x)) = \frac{d}{dx} \left[ 2(\omega + \omega_0)\Delta R(x; R_0)/c - i\kappa_x x \right] = 0 \quad (4.22)$$

In terms of the stationary points, the integral of Eq.(4.21) can be evaluated as

$$H(\kappa_x, \omega; R_0) = \sqrt{\frac{2\pi}{|\Phi'(x_*)|}} \exp(-i\Phi(x_*)) \quad (4.23)$$

Substituting from Eq.(4.14) the parabolic phase history into Eq.(4.22), we find that  $x_* = -\kappa_x R_0/c$  and we obtain the optimum transfer function  $H(\kappa_x, \omega; R_0)$  under the parabolic approximation as

$$H(\kappa_x, \omega; R_0) = F \exp\left\{-iR_0 \frac{c}{4} \frac{\kappa_x^2}{(\omega + \omega_0)}\right\} \quad \text{with} \quad F = \sqrt{\frac{\pi c R_0}{(\omega + \omega_0)}} \quad (4.24)$$

$F$  is a slowly varying function of  $\omega$  which in the case of narrow band SAR (i.e.,  $\omega_0/\omega \approx 1/10$ ) can be treated as constant. Using the hyperbolic phase history of Eq.(4.14) in Eq.(4.22), we find  $x_* = -[\kappa_x^2 R_0^2/(c^2 - \kappa_x^2)]^{1/2}$ , and the optimum transfer function results as

$$H(\kappa_x, \omega; R_0) = F \exp\left\{iR_0 \left[\sqrt{4(\omega + \omega_0)^2/c^2 + \kappa_x^2} - 2(\omega + \omega_0)/c\right]\right\} \quad (4.25)$$

$H(\kappa_x, \omega; R_0)$ , as given in Eq.(4.25), is known as the exact transfer function. The aim of SAR processing algorithms is to compensate the range dependent phase of the exact transfer function in an efficient manner for all ranges in the image. On the right side of Figure 4.2 the compressed point scatterer impulse response is shown, as it appears in the SAR image after ideal focusing. SAR image processing is well examined and several algorithms in different implementations can be found in the literature, [183],[184],[185],[186],[187],[188],[189]. Here, we decided to concentrate on a more fundamental interpretation of the SAR processing problem in a wave equation framework which will be given in the next two sections.

## 4.4 Radiating Reflector Model

An alternative approach for describing the operation of a pulsed radar can be addressed considering the scatterers in the scene as diffracting elements emitting the scattered EM field which is sampled by the SAR sensor along the sensor trajectory. This model is known in geophysics as the radiating reflector model [190],[191],[192]. Accordingly, the data acquisition process can be modelled by a number of diffracting elements placed on the ground which are supposed to emit all at the same time  $t = -t_0$ . The emitted field propagates in the medium with a constant velocity  $v$  towards the antenna and is measured along the sensor trajectory at time  $t = 0$  in intervals  $\Delta x$  corresponding the transmitter pulse repetition frequency  $f_{PRF}$

$$\Delta x = \frac{v}{f_{PRF}} \quad (4.26)$$

where  $v$  is the velocity of the sensor in the  $x$ -direction. The radiating reflector model supposes that the field sources are distributed on the ground and not on the sensor trajectory, where the

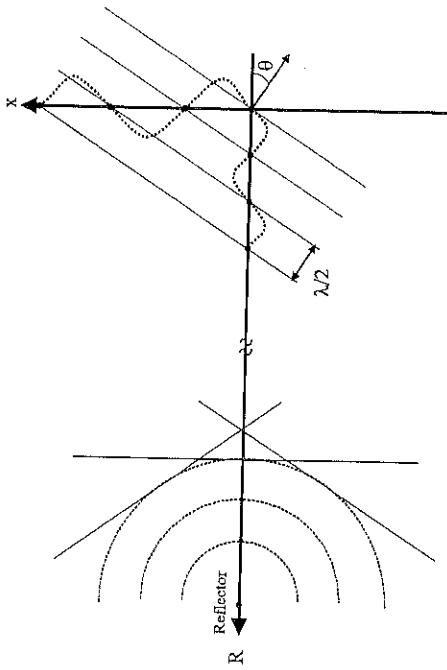


Figure 4.3: Data acquisition geometry under the radiating reflector model.

radar pulses are emitted in effect. Thus the sensor-scatterer distance is travelled once in the model, while in the real case it is travelled twice. To force the coincidence of the signal travel times, the velocity of wave propagation in the model is assumed to be half of the true value.

We consider a point source, located at  $P = P(x_0, R_0)$ , which radiates a spherical wave  $d(x, t)$  as shown in Figure 4.3. The radiated spherical wave can be represented by the superposition of monochromatic plane waves  $D(\kappa_x, \omega)$  orthogonal to the  $(x, R)$ -plane

$$d(x, t) = \frac{1}{(2\pi)^2} \iint D(\kappa_x, \omega) \exp i(\omega t + \kappa_x x) d\omega d\kappa_x \quad (4.27)$$

where  $D(\kappa_x, \omega)$  are the complex amplitudes of the plane waves, given by the two-dimensional Fourier transformation of  $d(x, t)$

$$D(\kappa_x, \omega; R=0) = \iint d(x, t; R=0) \exp -i(\omega t + \kappa_x x) dx dt \quad (4.28)$$

Each of these plane waves will reach the sensor trajectory under a different angle  $\theta$  at different times. For a given carrier angular frequency  $\omega_0$ , we can measure a spatial frequency  $\kappa_x$  in the  $x$ -direction and a spatial frequency  $\kappa_R$  in the  $R$ -direction. Both are dependent on the angle of incidence  $\theta$

$$\kappa_x = \frac{2}{c} \omega_0 \sin \theta = \frac{4\pi}{\lambda} \sin \theta \quad \text{and} \quad \kappa_R = \frac{2}{c} \omega_0 \cos \theta = \frac{4\pi}{\lambda} \cos \theta \quad (4.29)$$

so that

$$\kappa_x^2 + \kappa_R^2 = \frac{4\pi^2}{\lambda^2} = \frac{4\omega_0^2}{c^2} \rightarrow \omega = \frac{c}{2} \sqrt{\kappa_x^2 + \kappa_R^2} \quad (4.30)$$

The reconstruction of the point source from the acquired SAR data is based on the inversion of the propagation process. The propagation of each plane wave separately back to its emission point, using a two-dimensional wave equation, permits the evaluation of the source field at the emission time and provides an image of the point source. Under this view, the focused SAR image appears as a boundary value solution of the wave equation using the measured data as a boundary condition. The implementation of this idea will be the objective in the next section.

## 4.5 Plane Wave Focusing

Based on the considerations above, we address now the so-called wave equation or “ $\omega$ - $\kappa$ ” formulation of SAR processing. The wave equation formulation comes originally from the field of seismic data analysis, where the processing techniques as applied to seismic surveys show a strong similarity to those required to focus SAR data in azimuth [190],[194]. The following review of the “ $\omega$ - $\kappa$ ” processing focusing algorithm is inspired by [191],[192],[193]. The objective of this focusing procedure is to reconstruct the original wavefield  $d(x, t = -t_0; R)$ , emitted at time  $t = -t_0$  by the point sources in the scene using the measured wavefield  $d(x, t; R = 0)$  at  $R = 0$ . We assume that  $d(x, t; R = 0)$  is converted into the baseband and is range compressed. The first step is to decompose the measured field  $d(x, t = 0; R = R_0)$  into monochromatic plane waves performing the two-dimensional Fourier transformation of the raw data with respect to  $x$  and  $t$

$$d(x, t; R = 0) = \frac{1}{(2\pi)^2} \iint D(\kappa_x, \omega; R = 0) \exp i[(\omega + \omega_0)t + \kappa_x x] d\kappa_x d\omega \quad (4.31)$$

Each point in the two-dimensional frequency domain  $D(\kappa_x, \omega; R = 0)$  represents the complex amplitude of a monochromatic plane wave with a certain frequency travelling in a certain direction. Once the measured wavefield has been decomposed into plane waves, each component wave can be back-propagated to a particular range by simple multiplication with a complex exponential in order to reconstruct the emitted wavefield at time  $t = -t_0$ . For a plane wave, with a given  $\omega$  and  $\kappa_x$ , the phase operator required for the back-propagation from  $R = 0$  to  $R$  is  $\exp(i\kappa_R R)$ , where  $\kappa_{R_0} = 2\omega_0/c$ . Thus, the wavefield at depth  $R$  can be expressed in the  $(\kappa_x, \omega)$  domain as

$$D(\kappa_x, \omega; R) = D(\kappa_x, \omega; R = 0) \exp(i\kappa_R R) = D(\kappa_x, \omega; R = 0) \exp\left(i\left(\frac{2}{c} R_0 \sqrt{(\omega + \omega_0)^2 - \frac{c^2 \kappa_x^2}{4}}\right)\right) \quad (4.32)$$

Propagation of the wavefield at depth  $R$ , backwards in time by an amount of  $t_0$ , and inverse transformation of the result gives the wavefield  $d(x, t = -t_0; R)$  at the desired range, when the signal is emitted. Performing this operation for every value of range in the image, we find the focused image

$$d(x, t; R) = \frac{1}{(2\pi)^2} \iint D(\kappa_x, \omega; R = 0) \exp(i\kappa_R R) \exp i[(\omega + \omega_0)t + \kappa_x x] d\kappa_x d\omega \quad (4.33)$$

In the case of SAR data, the “data-receive-time-interval” is highly offset. For implementing the processing algorithm, it is convenient to shift the echo data window to the reference closest

approach range time  $t_0$ . Mathematically, this corresponds to a change of the range time variable from  $t$  to  $t' = t + t_0$  and is related to a shift of the range variable from  $R$  to  $R' = r + R_0$  with  $R_0 = ct_0/2$ . In the new coordinate system, Eq.(4.33) can be written as a function of the Fourier transformation of the original data as

$$d(x, t'; R = 0) = \frac{1}{(2\pi)^2} \iint D(\kappa_x, \omega, R = 0) \exp[i\kappa_x(R + R_0)] \exp[i\kappa_x x + (\omega + \omega_0)(t - t_0)] d\kappa_x d\omega \quad (4.34)$$

The drawback of Eq.(4.34) is that  $d(x, t = -t_0; R)$  is not expressed as an inverse Fourier transformation with respect to  $\kappa_x$  and  $\kappa_R$ . Thus, the straightforward computation of the double integral is too time consuming to be of practical interest.

Assuming the propagation velocity to be constant, Eq.(4.34) can be transformed into a two-dimensional Fourier transformation introducing a  $\kappa_x$  dependent mapping of the data from the  $\omega$ -domain into the  $\kappa_R$ -domain, known as Stolt mapping [195]

$$\omega = \frac{c}{2} \sqrt{\kappa_x^2 + (\kappa_R + 2\omega_0/c)^2} - \omega_0 \quad (4.35)$$

According to Eq.(4.35), lines of constant  $\omega$  in the  $(\kappa_x, \omega)$  space are mapped into circles centered at  $(\kappa_x = 0, \kappa_R = -2\omega_0/c)$  in the  $(\kappa_x, \kappa_R)$  space [187]. Defining the Stolt mapping operator  $S\{\cdot\}$  as a mapping from  $\omega$  to  $\kappa_R$ , controlled by Eq.(4.35), Eq.(4.34) can be written as

$$\tilde{t}(x, R + R_0) = \iint I(\kappa_x, \kappa_R) \exp i(\omega t + \kappa_R r) d\kappa_x d\kappa_R \quad (4.36)$$

with

$$I(\kappa_x, \kappa_R) = QS\{D(\kappa_x, \omega)\} \exp(i\kappa_R R_0) \exp[-i(R_0 \sqrt{\kappa_x^2 + (\kappa_R + 2\omega_0/c)^2})] \quad (4.37)$$

where

$$S\{D(\kappa_x, \omega)\} = \tilde{D}(\kappa_x, \frac{c}{2} \sqrt{\kappa_x^2 + (\kappa_R + \kappa_{R_0})^2}) \quad \text{and} \quad Q = \frac{\kappa_R c}{2\sqrt{\kappa_x^2 + (\kappa_R + 2\omega_0/c)^2}} \quad (4.38)$$

Eqs.(4.36-38) address the SAR focusing process as a four stage two-dimensional Fourier transformation problem: 1) Transformation of the range compressed data in the  $(\kappa_x, \omega)$  space, 2) transformation from the  $(\kappa_x, \omega)$  into the  $(\kappa_x, \kappa_R)$  space via the Stolt mapping, 3) multiplication with a global two-dimensional phase term, and 4) inverse two-dimensional Fourier transformation. An alternative formulation can be made by interchanging the order of stage 2) and 3), i.e., performing the multiplication with the two-dimensional phase term in the  $(\kappa_x, \omega)$  space and then applying the Stolt mapping

$$U(\kappa_x, \kappa_R) = QS\{D(\kappa_x, \omega) \exp\{iR_0[\sqrt{4(\omega + \omega_0)^2/c^2 + \kappa_x^2} - 2(\omega + \omega_0)/c]\}\} \quad (4.39)$$

The two-dimensional phase term in the  $(\kappa_x, \omega)$  space equals the phase term of the exact transfer function as given in Eq.(4.25) underlying the equivalence of both considerations [187].

The problem with this plane wave focusing method lies in the nonlinear Stolt mapping operation. The raw data are spaced uniformly in the  $\omega$ -domain. To obtain samples uniformly spaced in the  $\kappa_R$ -domain the Stolt mapping requires a critical interpolation in order to resample the data in the  $\omega$  domain. The required interpolation can be expressed as a shift and a scaling of the range frequency  $\omega$  axis as a function of the azimuth frequency  $\kappa_x$ . If the scaling is ignored, the Stolt mapping operation can be replaced by an  $\omega$ -independent shift operation performed by a simple multiplication with a linear phase function before transforming in the  $(\kappa_x, \omega)$  space. By this approximation only the wavenumbers corresponding to a single frequency  $\omega = 0$  are mapped correctly. This realization of the processing algorithm is known as the monochromatic wavenumber approach [193],[187].

## 4.6 SAR System Model

Up to now, we restricted our considerations on deterministic scatterers, i.e., point scatterers, modelled as a three-dimensional Dirac delta function weighted with the appropriate radar cross section  $\sigma$  [196]

$$\sqrt{\sigma} \delta(\vec{r} - \vec{r}') \quad (4.40)$$

where  $\vec{r}'$  is the position vector of the scatterer in the three-dimensional space. In contrast to deterministic scatterers, the most natural terrain surfaces are distributed scatterers characterised by a random space and/or time dependent scattering behaviour. Such scatterers are described by means of a complex reflectivity function  $\tilde{u}(\vec{r})$  [197],[198],[199]. Assuming many independent scattering elements within the resolution cell, the complex reflectivity function becomes a zero-mean circular Gaussian white noise process [199],[200],[201]. The statistical properties of the scatterer are then expressed by its autocorrelation function

$$\langle \tilde{u}(\vec{r}) \tilde{u}^*(\vec{r}') \rangle = \sigma_v(\vec{r}) \delta(\vec{r}' - \vec{r}) \quad (4.41)$$

where  $\sigma_v(\vec{r})$  is known as the volume scattering coefficient [99]. The autocorrelation of Eq.(4.41) is non-stationary in order to represent non-homogeneous distributed scatterers with spatially varying scattering coefficients. In general, the received signal consists of both, a deterministic and a random contribution.

The process of SAR data acquisition can be interpreted as the geometric projection of the three-dimensional complex terrain reflectivity  $\tilde{u}(\vec{r}) = \tilde{u}(x, y, z)$ , from the three-dimensional object space into the two-dimensional azimuth/range radar image coordinate system according [202],[203],[204]

$$u(x, R) = \int \tilde{u}(x, y_0 + R \sin \theta, z_0 - R \cos \theta) R d\theta \quad (4.42)$$

where  $(x, y_0, z_0)$  are the sensor coordinates,  $\theta$  the radar look angle, and  $\tilde{u}(x, R)$  is the two-dimensional projection of the complex reflectivity function along  $R d\theta$  into the  $(x, R)$ -plane (see

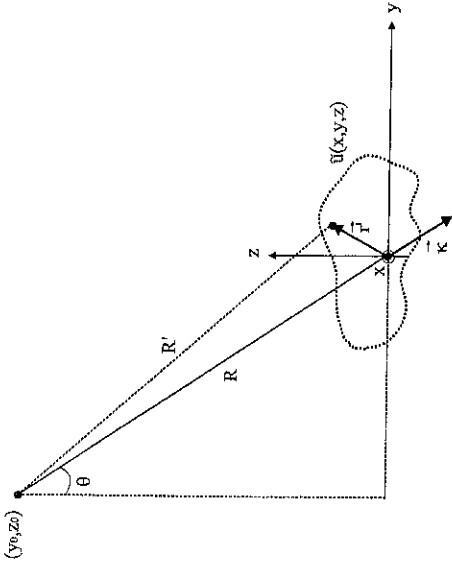


Figure 4.4: On the SAR system model.

Figure 4.4). It is exactly this projection which causes the typical geometrical distortions in SAR images: while the  $x$ -coordinate is not affected, all points at the same range distance  $R$  to the sensor are projected into the same point in the SAR image, and therefore, are no longer distinguishable.

The SAR image, as discussed in Section 4.3, is formed by the two-dimensional correlation of the measured signal with the point scatterer impulse response  $h(x, t)$

$$i(x, R) = u(x, R) \exp(-2i\kappa R) \odot_x \odot_t h(x, t) + n(x, R) \quad (4.43)$$

where  $n$  is a zero-mean circular Gaussian white noise process, representing the additive noise component in the image. Ignoring range migration, the range  $R$  and range-time  $t$  coordinates become interchangeable, and the two-dimensional correlation can be rewritten in terms of the range coordinate  $R$  as

$$\begin{aligned} i(x, R) &= u(x, R) \exp(-2i\kappa R) \odot_x \odot_R h(x, R) + n(x, R) \\ &= \iint u(x', R') \exp(-2i\kappa R') h(x - x', R - R') dx' dR' + n(x, R) \end{aligned} \quad (4.44)$$

The primed coordinates are related to the scatterer, while the unprimed coordinates are related to a reference point for the impulse response  $h(x, R)$ . Substituting Eq.(4.42) into Eq.(4.44), we obtain the processed SAR image in form of a bandpass filtered projection of the complex reflectivity function [206]

$$i(x, R) = \left( \exp(-2i\kappa R) \int \tilde{u}(x, y_0 + R \sin \theta, z_0 - R \cos \theta) R d\theta \right) \odot_x \odot_t h(x, R) + n(x, R) \quad (4.45)$$

Eq.(4.45) may be restated in terms of a volume integral as

$$i(x, R) = \int_V \tilde{u}(\vec{r}') \exp(-2i\kappa R') h(x - x', R - R') dV' + n(x, R) \quad (4.46)$$

where  $dV' = dx' dy' dz'$ . At this point, it is convenient to develop a far-field plane wave approximation of Eq.(4.46) [204],[205]. Considering a sufficient small neighbourhood around the scattering point, in which the look angle  $\theta$  may be assumed to be constant, we approximate

$$R'(y', z') = R + \Delta R(y', z') \approx R + [(y' - y) \sin \theta + (z' - z) \cos \theta] = R + \vec{\kappa} \cdot \vec{r}' \quad (4.47)$$

where  $\vec{r}'$  indicates the position of the effective scatterer inside the resolution element. The wave vector  $\vec{\kappa}$  lies in the radar line-of-sight direction, and thus, is dependent on the look angle  $\theta$

$$\vec{\kappa} = [\kappa_x, \kappa_y, \kappa_z]^T = \kappa [0, \sin \theta, -\cos \theta]^T \quad (4.48)$$

Substituting Eq.(4.47) into the volume integral of Eq.(4.46), we finally obtain

$$i(x, R) = \exp(-i2\kappa R) \int_V \tilde{u}(\vec{r}') \exp(-2i\vec{\kappa} \cdot \vec{r}') h(x - x', R - R') dV' + n(x, R) \quad (4.49)$$

$$= \left( \exp(-2i\kappa R) \int \tilde{u}(x, y_0 + R \sin \theta, z_0 - R \cos \theta) R d\theta \right) \odot_x \odot_t h(x, R) + n(x, R) \quad (4.50)$$

The significance of Eqs.(4.49-50) is that they express the imaging process as the projection of the effective scatterers inside the resolution cell onto the line-of-sight direction. The phase of a point (pixel) in the SAR image depends both on the projection  $\vec{\kappa} \cdot \vec{r}'$  of the scatterer location onto the line-of-sight direction and on the integral of the complex reflectivity function normal to the  $(x, R)$ -plane. This will be of importance in SAR interferometry.

## 4.7 SAR Interferometry

Across-Track SAR interferometry is a technique that allows the extraction of topographic information by means of SAR [206],[207],[208],[209]. It is based on the generation of an interferogram between two complex SAR images of the same area acquired from two spatially separated radar antennas. The two images can either be acquired by using two antennas on the same platform simultaneously (single-pass interferometry), or by using one antenna in repeated passes over the same area at different times (repeat-pass interferometry). In the following, we will briefly summarise the basic principle of SAR interferometry using a geometrical approach. For this we consider two antennas  $S_1$  and  $S_2$ , separated by a baseline  $B$ , observing the same scene. A point  $P$  is located within the scene at a height  $z$ , as shown in Figure 4.5. The range distances of the two antennas to the scatterer are  $R$  and  $R + \Delta R$ , respectively. The receiving signals  $s_1$  and  $s_2$ , after SAR processing, consist of the complex terrain reflectivity  $u(R)$  modulated by a phase term due to range distance to the scatterer

$$s_1(R) = u_1(R) \exp(i\phi(R)) \quad \text{and} \quad s_2(R + \Delta R) = u_2(R + \Delta R) \exp(i\phi(R + \Delta R)) \quad (4.51)$$

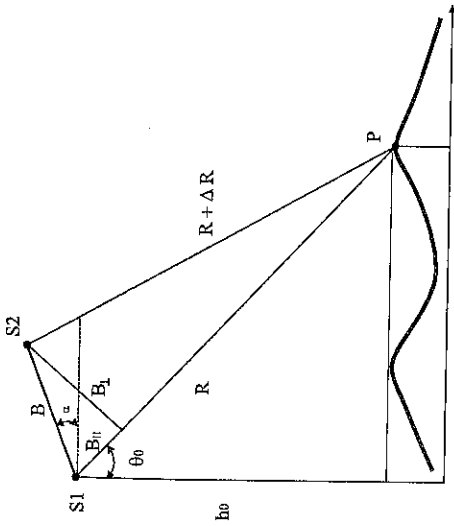


Figure 4.5: InSAR imaging geometry.

The phase of the received signals consists of two contributions: a deterministic one associated to the round trip path lengths, and a random phase contribution due to the different terrain reflectivity characteristics

$$\varphi_1 = 2\frac{2\pi}{\lambda}R + \arg\{u_1\} \quad \text{and} \quad \varphi_2 = 2\frac{2\pi}{\lambda}(R + \Delta R) + \arg\{u_2\} \quad (4.52)$$

The factor of two is necessary in repeat-pass configurations to account that both transmitting and receiving paths are unique for each acquisition. The knowledge of the two antenna locations and of the corresponding range distances permits the determination of the location of the point  $P$  in the three-dimensional space by simple triangulation. The accuracy depends on the precision of estimation of these parameters. After coregistration of the two images, [89],[210], (because of the angular diversity the two SAR images are not exactly overlapping), a complex interferogram is formed multiplying the first signal with the complex conjugate of the second signal as

$$s_1(R)s_2^*(R + \Delta R) = |s_1 s_2^*| \exp i(\varphi_1 - \varphi_2) = |s_1 s_2^*| \exp(-i\frac{4\pi}{\lambda}\Delta R) \quad (4.53)$$

Assuming the same random phase contributions in both images, i.e.,  $\arg\{u_1\} = \arg\{u_2\}$ , they cancel out when the interferogram is formed. Thus, although the phase of each single image separately is random, the phase of the interferogram is deterministic, corresponding to the path difference of the two signals  $\Delta R$

$$\phi = -\frac{4\pi}{\lambda}\Delta R + 2\pi N \quad \text{where} \quad N = 0, \pm 1, \pm 2, \dots \quad (4.54)$$

Because of the short wavelength, the phase is measured only as the modulus  $2\pi$  of the absolute phase difference. Foreseeing the  $2\pi$  ambiguity, Eq.(4.54) manifests the main advantage of SAR

interferometry: The range difference  $\Delta R$  is measured in terms of the interferometric phase with a sensitivity of the order of fractions of the wavelength. Therefore, the interferometric technique is potentially much more accurate than conventional triangulation techniques.

Using the cosine law,  $\Delta R_A$  may be expressed in terms of the imaging geometry parameters as

$$(R + \Delta R)^2 = R^2 + B^2 - 2RB \cos(\pi/2 - \theta_0 + \alpha) = R^2 + B^2 + 2RB \sin(\theta_0 - \alpha) \rightarrow \quad (4.55)$$

$$\sin(\theta_0 - \alpha) = \frac{(R + \Delta R)^2 - R^2 - B^2}{2RB} \quad (4.56)$$

where  $\theta_0$  is the reference look angle of the first antenna and  $\alpha$  the angle of the baseline with respect to the horizontal. The height  $h$  of the Point  $P$  is given by

$$h = h_0 - R \cos \theta_0 \quad (4.57)$$

Eq.(4.54), Eq.(4.56), and Eq.(4.57), constitute a nonlinear system of three equations with three unknowns: the range path difference  $\Delta R$ , the radar look angle  $\theta_0$ , and the local height  $h$ . Thus the height  $h$  arises from the measured interferometric phase  $\Delta\phi$ , through the estimation of the look angle  $\theta_0$  for each resolution cell in the interferogram. Applying this over the entire image we obtain finally an elevation model with the same spatial resolution as the original SAR images. Unfortunately, SAR interferometry is by no means a task as easy as it may appear. There are some critical points that need to be overcome in order to extract the terrain height from the two SAR images. The fact that the interferometric phase is measured only modulo  $2\pi$  makes the determination of the absolute phase necessary. A large number of different procedures addressing solutions to this problem, known as phase unwrapping algorithms, have been addressed in the literature [211],[212],[213],[214],[215],[216],[217],[218]. In general, the ability to resolve the 2 ambiguities depends on the local terrain slope and on the phase noise level caused by signal decorrelation between the two acquired images [101],[219].

The most critical factor in the application of SAR interferometry is the quality of the interferometric phase, which is degraded by any amount of noise in the interferogram. The reason for the appearance of noise in the interferogram is the decorrelation of the two images [220]. A measure of the phase noise is the interferometric coherence  $\gamma$  which is defined as the absolute value of the normalised complex cross-correlation between both signals

$$\gamma := \frac{|< s_1 s_2^* >|}{\sqrt{< s_1 s_1^* > < s_2 s_2^* >}} \quad (4.58)$$

For practical evaluation of  $\gamma$ , the expectation operator in Eq.(4.58) is replaced by spatial averaging [222],[223]. The interferometric coherence varies between 0 and 1. It becomes a maximum if both signals are identical ( $\gamma = 1$ ), and vanishes if the two signals do not correlate ( $\gamma = 0$ ). Consequently, the achievable accuracy of the estimation of the interferometric phase is reduced by any loss in coherence. Apart from processing artifacts, decorrelation may occur due to system noise in both signals. In the case of distributed scatterers, geometrical decorrelation due to the difference of look angles introduces noise in the interferogram and corrupts the estimation of the interferometric phase. In the repeat-pass case, temporal decorrelation of the scene



due to changes in the backscatter behaviour between the two observations, reduces the signal correlation and leads to a randomisation of the phase [221]. A more detailed evaluation of the interferometric coherence will be given in Section 4.9. Furthermore, the performance of an interferometric system depends on the radar sensor parameters, the accuracy of the orbit or flight-track estimation, and on the quality of the applied processing procedures [63].

## 4.8 Interpretation of the Interferometric Phase

For the application of interferometry, it is important to analyse the information content of the interferogram. For this, we proceed with our geometrical description, focusing now on the evaluation of the interferometric phase. Neglecting  $\Delta R^2$  on the left side of Eq.(4.55), the range difference  $\Delta R$  may be approximated as

$$\Delta R = \frac{B^2}{2R} + B \sin(\theta_0 - \alpha) \quad (4.59)$$

If the baseline  $B$  is small compared to the slant range distance  $R$ , as it is the case for spaceborne interferometric systems where  $B$  is of the order of hundred meters while  $R$  is of the order of several hundred kilometers, the first term on the right side of Eq.(4.59) can be neglected

$$\Delta R \approx B \sin(\theta_0 - \alpha) \quad (4.60)$$

Eq.(4.60) is known as the parallel ray approximation [60]. It is an inaccurate approximation for satellite geometries with large swaths and becomes invalid for airborne geometries, but it is still good enough for our purposes. Furthermore, it is common to decompose the baseline  $B$  into a parallel  $B_{\parallel}$  and orthogonal  $B_{\perp}$  to the line-of-sight or range direction component

$$B_{\parallel} = B \sin(\theta_0 - \alpha) \quad \text{and} \quad B_{\perp} = B \cos(\theta_0 - \alpha) \quad (4.61)$$

Substituting now Eq.(4.60) into Eq.(4.54), by using Eq.(4.61), we transform the interferometric phase into a more suitable form

$$\phi = -\frac{4\pi}{\lambda} B \sin(\theta_0 - \alpha) = -\frac{4\pi}{\lambda} B_{\parallel} \quad (4.62)$$

The phase  $\phi$ , as given in the last equation, contains both information about the range distance and about the height of  $P$ . To make this more clear, we consider in a first scenario, a second point  $P'$  located at the same height  $z$  as  $P$ , but at a different range distance  $R + \Delta R$ , as shown in Figure 4.6.a. The look angle will change about  $\Delta\theta_R$ , and according to Eq.(4.62), the corresponding interferometric phase of  $P'$  is

$$\phi' = -\frac{4\pi}{\lambda} B \sin(\theta_0 + \Delta\theta_R - \alpha) \quad (4.63)$$

The phase difference between the two points in the interferogram is given by

$$\Delta\phi_R = \phi' - \phi = -\frac{4\pi}{\lambda} B [\sin(\theta_0 + \Delta\theta_R - \alpha) - \sin(\theta_0 - \alpha)] \approx -\frac{4\pi}{\lambda} B \sin(\theta_0 - \alpha) \Delta\theta_R \quad (4.64)$$

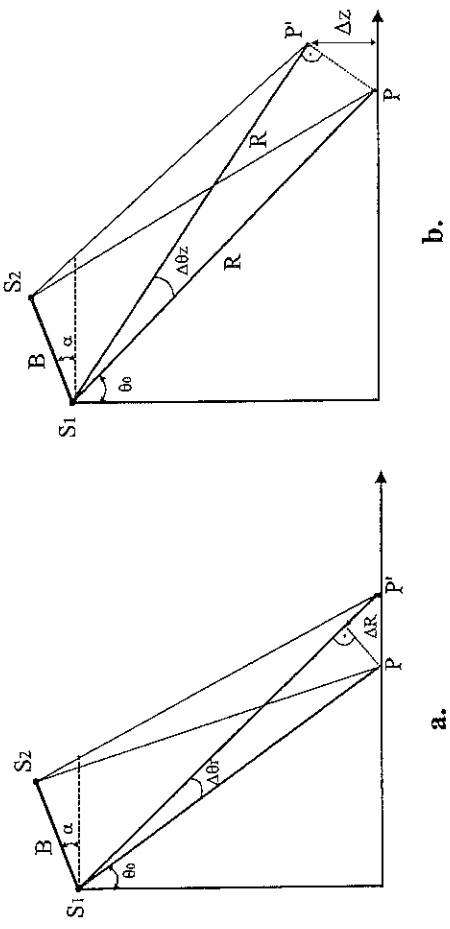


Figure 4.6: Geometry for the interpretation of the interferometric phase.

Applying a small angle approximation,  $R\Delta\theta_R \approx R \sin \Delta\theta_R = \Delta R / \tan \theta_0$ , the phase difference between the two points in the interferogram as a function of their range difference  $\Delta R$  becomes

$$\Delta\phi_R = -\frac{4\pi}{\lambda} \frac{B \sin(\theta_0 - \alpha) \Delta R}{R \tan \theta_0} = -\frac{4\pi}{\lambda} \frac{B_{\parallel} (\Delta R)}{R \tan \theta_0} \quad (4.65)$$

Eq.(4.65) states that a flat surface without topography generates a linear interferometric phase known as flat-earth phase component. This linear term has to be subtracted in order to relate directly the interferometric phase to the topography.

In a second scenario now, we consider the point  $P'$  to be located at the same range distance  $R$  as  $P$ , but at different height  $z + \Delta z$  as shown in Figure 4.6.b. The look angle will alter by  $\Delta\theta_z$ , and the phase in the interferogram will be

$$\phi' = -\frac{4\pi}{\lambda} B \sin(\theta_0 + \Delta\theta_z - \alpha) \quad (4.66)$$

According to our previous considerations, in order to obtain the excessive phase contribution caused by the height difference between the two points, we have to subtract the range dependent phase component

$$\Delta\phi_z = \phi' - \phi = -\frac{4\pi}{\lambda} B [\sin(\theta_0 + \Delta\theta_z - \alpha) - \sin(\theta_0 - \alpha)] \approx \frac{4\pi}{\lambda} B \sin(\theta_0 - \alpha) \Delta\theta_z \quad (4.67)$$

Finally, using again  $\Delta\theta_z \approx R \sin \Delta\theta_z = \Delta z / \sin \theta_0$ , the interferometric phase difference related to the height variation  $\Delta z$ , results as

$$\Delta\phi_z = -\frac{4\pi}{\lambda} \frac{B \sin(\theta_0 - \alpha) \Delta z}{R \sin \theta_0} = -\frac{4\pi}{\lambda} \frac{B_{\perp} \Delta z}{R \sin \theta_0} \quad (4.68)$$

The height sensitivity of the interferometric phase follows as

$$\frac{\Delta\phi_z}{\Delta z} = -\frac{4\pi}{\lambda} \frac{B_\perp}{R \sin \theta_0} \quad (4.69)$$

For example, in the case of a spaceborne system ( $R = 300\text{Km}$ ) operating at L-band with a phase resolution of  $3^\circ$ , and an imaging geometry with a baseline of  $B_\perp = 100\text{m}$  and look angle  $\theta_0 = 30^\circ$ , the theoretical height resolution is in the order of  $1.5\text{m}$ . The so-called  $2\pi$  ambiguity height, i.e., the height difference corresponding to a phase difference of  $2\pi$ , is then

$$\Delta z_{2\pi} = -\frac{\lambda}{2} \frac{R \sin \theta_0}{B_\perp} \quad (4.70)$$

For the same configuration as used in the example before,  $\Delta z_{2\pi}$  is of the order of  $180\text{m}$ . According to Eq.(4.69), the height sensitivity is directly proportional to the wavelength and reciprocal to the baseline. The use of small wavelengths (X- or C-band) is advantageous for the height resolution of the interferometric system, and it is preferably used in one-pass interferometric systems. On the other hand, in the case of repeat-pass interferometric systems, small wavelengths are affected stronger by temporal decorrelation than longer wavelengths (L- or P-band) [101],[102],[93]. Large baselines have the same effect as short wavelengths concerning the height resolution, but as it will be shown in the next section, the use of large baselines implies geometrical decorrelation which can only be partially compensated.

## 4.9 Interferometric System Model

Up to now, we summarised the basic rationale of SAR interferometry using an ordinary geometrical interpretation. In order to deepen our physical understanding of SAR interferometry, we need a more sophisticated model description [99],[204]. Returning to our considerations in Section 4.6, we express now the two interferometric SAR images in form of their volume scattering integral as

$$i_1(x_1, R_1) = \exp(-i\kappa_1 R_1) \int_V \tilde{u}_1(\vec{r}') \exp(-2i\tilde{\kappa}_1 \cdot \vec{r}') h(x_1 - x', R_1 - R_1') dV' + n_1(x_1, R_1) \quad (4.71)$$

$$i_2(x_2, R_2) = \exp(-i\kappa_2 R_2) \int_V \tilde{u}_2(\vec{r}') \exp(-2i\tilde{\kappa}_2 \cdot \vec{r}') h(x_2 - x', R_2 - R_2') dV' + n_2(x_2, R_2) \quad (4.72)$$

The wavevectors  $\tilde{\kappa}_1$  and  $\tilde{\kappa}_2$  are functions of the corresponding radar look angles  $\theta_1$  and  $\theta_2$

$$\tilde{\kappa}_1 = |\tilde{\kappa}_1| [0, \sin \theta_1, -\cos \theta_1]^T \quad \text{and} \quad \tilde{\kappa}_2 = |\tilde{\kappa}_2| [0, \sin \theta_2, -\cos \theta_2]^T \quad (4.73)$$

Although, conventional interferometers operate at a fixed central frequency,  $|\tilde{\kappa}_1| = |\tilde{\kappa}_2|$ , for our analysis here it is convenient to allow the acquisition of the two images using slightly different frequencies,  $|\tilde{\kappa}_1| \neq |\tilde{\kappa}_2|$ . It is important to realise that, because of the different acquisition angles, the two images contain different projections of the complex reflectivity function.

The coregistration of the second image with respect to the first image, forcing in azimuth  $x_2 = x_1 = x$  and in range  $R_2 = R_1 = R$  (see Eq.(4.60)), is necessary for an optimal overlap of the two impulse response functions

$$i_2(x, R_2) = \exp(-i\kappa_2 R_2) \int_V \tilde{u}_1(\vec{r}') \exp(-2i\tilde{\kappa}_2 \cdot \vec{r}') h(x - x', R_2 - R_2') dV' \quad (4.74)$$

After coregistration, the interferogram is formed by multiplying the first image  $i_1(x, R_1)$  with the complex conjugate of the second image  $i_2^*(x, R_2)$ . In general, the complex reflectivities  $\tilde{u}_1(\vec{r})$  and  $\tilde{u}_2(\vec{r})$  are not identical as the scatterer may have changed in a time interval between the two acquisitions. Therefore, they have to be considered only partially correlated

$$\langle \tilde{u}_1(\vec{r}) \tilde{u}_2^*(\vec{r}') \rangle = \sigma_{ue}(\vec{r}) \delta(\vec{r}' - \vec{r}) \quad (4.75)$$

The effective volume scattering coefficient  $\sigma_{ue}$  expresses the amount of correlation of the two complex reflectivities [99],[100]. Since noise and signal are uncorrelated, the expected interferometric response, given by the complex cross-correlation of the two SAR images, becomes

$$\langle i_1(x, R_1) i_2^*(x, R_2) \rangle = \exp(-i\Phi) \int_V \sigma_{ue}(\vec{r}') \exp\{-2i(\tilde{\kappa}_1 - \tilde{\kappa}_2) \cdot \vec{r}'\} h(x - x', R_1 - R_1')^2 dV' \quad (4.76)$$

where  $\Phi = 2(\kappa_1 R_1 - \kappa_2 R_2)$ . Furthermore, taking into account Eq.(4.41), we obtain the signal intensities of the two SAR images as

$$\langle i_1(x, R_1) i_1^*(x, R_1) \rangle = \int_V \sigma_{v1} |h(x - x', R_1 - R_1')|^2 dV' + N_1 \quad (4.77)$$

$$\langle i_2(x, R_2) i_2^*(x, R_2) \rangle = \int_V \sigma_{v2} |h(x - x', R_2 - R_2')|^2 dV' + N_2 \quad (4.78)$$

where  $N = E\{n_i n_i^*\}$  denotes the noise power. Using Eqs.(5.76-78) in the definition of the interferometric coherence in Eq.(4.58), and assuming for simplicity the individual image intensities to be equal,  $\sigma_{v1} = \sigma_{v2} = \sigma_v$ , we obtain

$$\gamma = \frac{\int_V \sigma_{ue}(\vec{r}') \exp\{-2i(\tilde{\kappa}_1 - \tilde{\kappa}_2) \cdot \vec{r}'\} |h(x - x', R - R')|^2 dV'}{\int_V \sigma_v |h(x - x', R - R')|^2 dV'} \quad (4.79)$$

Simple extension of the nominator and the denominator in Eq.(5.79) leads to a decomposition of the interferometric coherence into the following contributions

$$\gamma = \gamma_{SNR} \gamma_{\text{temporal}} \gamma_{\text{spatial}} \quad (4.80)$$

- $\gamma_{SNR}$  represents the decorrelation caused by additive noise. Assuming the same Signal-to-Noise ratio (SNR) in both images,  $\gamma_{SNR}$  is given by [220]

$$\gamma_{SNR} = \frac{\int_V \sigma_v(\vec{r}') |h(x-x', R-R')|^2 dV'}{\int_V \sigma_v(\vec{r}') |h(x-x', R-R')|^2 dV' + N} = \frac{1}{1 + (SNR)^{-1}} \quad (4.81)$$

- $\gamma_{Temporal}$  is the temporal decorrelation caused by changes in the scatterer geometry and/or changes in the backscattering behaviour of the scatterers within the resolution cell occurring during the time interval between the two acquisitions

$$\gamma_{Temporal} = \frac{\int_V \sigma_v(\vec{r}') |h(x-x', R-R')|^2 dV'}{\int_V \sigma_v(\vec{r}') |h(x-x', R-R')|^2 dV'} \quad (4.82)$$

If  $\sigma_v(\vec{r}) = \sigma_v(\vec{r}')$ ,  $\gamma_{Temporal}$  becomes 1. On the other extreme, if the  $\tilde{w}_1(\vec{r}')$  and  $\tilde{w}_2(\vec{r}')$  are completely uncorrelated,  $\sigma_v(\vec{r}) = 0$ , and consequently  $\gamma_{Temporal}$  becomes 0.

- $\gamma_{Spatial}$  expresses decorrelation due to the different projection perspective caused by the different look angles so that the two SAR images are acquired

$$\gamma_{Spatial} = \frac{\int_V \sigma_v(\vec{r}') \exp\{-2i(\tilde{\kappa}_1 - \tilde{\kappa}_2) \cdot \vec{r}'\} |h(x-x', R-R')|^2 dV'}{\int_V \sigma_v(\vec{r}') |h(x-x', R-R')|^2 dV'} \quad (4.83)$$

Eq.(4.83) makes it evident, that the difference in the look angles, expressed in terms of different wave vectors  $\tilde{\kappa}_1$  and  $\tilde{\kappa}_2$ , introduces a decorrelation in the interferogram. The physical reason for this lies in the variation of the coherent sum of the backscattered signal from the individual scatterers within the resolution cell with aspect angle.

For a better understanding of the spatial decorrelation, we need to evaluate the vector product in the exponential term of Eq.(4.83). Using  $\Delta\kappa = \kappa_1 - \kappa_2$ , we restate  $\kappa_1 = \kappa + \Delta\kappa/2$  and  $\kappa_2 = \kappa - \Delta\kappa/2$ , so that

$$\begin{aligned} (\tilde{\kappa}_1 - \tilde{\kappa}_2) \cdot \vec{r}' &= \kappa(\sin\theta_1 - \sin\theta_2)y' + (\Delta\kappa/2)(\sin\theta_1 + \sin\theta_2)y' - \\ &\quad \kappa(\cos\theta_1 - \cos\theta_2)y' - (\Delta\kappa/2)(\cos\theta_1 + \cos\theta_2)y' \\ &\approx (\kappa\Delta\theta \cos\theta - \Delta\kappa \sin\theta)y' + (\kappa\Delta\theta \sin\theta + \Delta\kappa \cos\theta)z' \end{aligned} \quad (4.84)$$

Employing once again the small angle approximation  $\Delta\theta \approx \sin\Delta\theta = B_\perp/R$ , where  $B_\perp$  is the orthogonal component of the baseline, we finally obtain

$$\exp\{-i2(\tilde{\kappa}_1 - \tilde{\kappa}_2) \cdot \vec{r}'\} = \exp -i2 \left[ \left( \frac{\kappa B_\perp \cos\theta}{R} - \Delta\kappa \sin\theta \right) y' + \left( \frac{\kappa B_\perp \sin\theta}{R} + \Delta\kappa \cos\theta \right) z' \right] \quad (4.85)$$

Substituting Eq.(4.85) into Eq.(4.83), the spatial coherence term may be split into two further contributions

$$\gamma_{Spatial} = \gamma_{Range} \gamma_{Volume} \quad (4.86)$$

where  $\gamma_{Range}$  expresses the decorrelation with respect to a reference plane  $(x, y)$  (on which  $h(x-x', R-R')$  is referred)

$$\gamma_{Range} = \frac{\left| \int \exp\left\{-2i\left(\frac{\kappa B_\perp \cos\theta}{R} - \Delta\kappa \sin\theta\right)y'\right\} |h(x-x', R-R')|^2 dx' dy' \right|}{\int |h(x-x', R-R')|^2 dx' dy'} \quad (4.87)$$

and  $\gamma_{Volume}$  represents the decorrelation caused by the height distribution of  $\sigma_{ve}(z)$  above the reference plane

$$\gamma_{Volume} = \frac{\left| \int \sigma_{ve}(z') \exp\left\{-2i\left(\frac{\kappa B_\perp \sin\theta}{R} + \Delta\kappa \cos\theta\right)z'\right\} dz' \right|}{\int \sigma_{ve}(z') dz'} \quad (4.88)$$

The first  $y'$ -dependent contribution can always be eliminated from the interferogram by choosing  $\Delta\kappa$  so that

$$\Delta\kappa = \frac{\kappa B_\perp}{R \tan\theta} = \frac{2\pi}{\lambda} \frac{B_\perp}{R \tan\theta} \quad (4.89)$$

For tunable interferometric systems, capable to operate at different central frequencies, the coherence  $\gamma_{Range}$  can be optimised choosing  $\Delta\kappa$  with respect to the actual baseline according to Eq.(4.89) [224],[225]. In the case of conventional interferometric systems, operating at a fixed central frequency, the effect of  $\gamma_{Range}$  may be eliminated by filtering the bandwidth of the two SAR images at different central frequencies before forming the interferogram, taking into account a degradation of spatial range resolution. This procedure is known as wavenumber or spectral filtering [224],[225]. Total decorrelation occurs when the spectral shift exceeds the available system bandwidth  $W$  ( $\Delta\kappa = 2\pi W/c$ ). The corresponding baseline is known as the critical baseline  $B_{LC}$

$$B_{LC} = \frac{\lambda W R \tan\theta}{c} \quad (4.90)$$

Recapitulating, in the case of pure surface scattering, the spatial decorrelation may be eliminated by common band filtering of the range spectra [225]. However any finite height distribution of the scatterers inside the resolution cell leads to volume decorrelation which cannot be removed by applying spectral filtering. According to Eq.(4.89), the spectral shift  $\Delta\kappa$  varies inversely to the wavelength. Thus, for a given imaging geometry, systems operating at smaller wavelengths are more sensitive to spatial decorrelation than longer wavelength systems. From the polarisation point of view,  $\gamma_{SNR}$  can be considered to be independent of the used polarisation, because noise does not have any polarimetric structure. On the contrary, the other two coherence contributions,  $\gamma_{Temporal}$  and  $\gamma_{Spatial}$ , are strongly dependent on wave polarisation as we will show in the next chapter.

## 4.10 Differential Interferometry

In the previous sections, we considered SAR interferometry as a technique for the generation of high resolution topographic maps. In the last section of this chapter, we introduce a development

of the basic interferometric scheme for the detection and mapping of dynamic deformations. For this we consider the situation of two SAR observations of the same area at different times, supposing a dynamic deformation of the scene in the time between the two observations [86],[89]. In the first image, acquired before the deformation process is occurring, the received signal form a point P in the scene (see Figure 4.7) is

$$s_1(R_1) = |s_1(R_1)| \exp\left(\frac{4\pi}{\lambda} R_1\right) \quad (4.91)$$

In the second image, acquired after the deformation is occurring, the corresponding received signal form the point P is

$$s_2(R_2) = |s_2(R_2)| \exp\left(\frac{4\pi}{\lambda} (R_2 + \Delta R_d)\right) \quad (4.92)$$

The interferometric phase of an interferogram, formed using the two images, contains in addition i.e., to the topographic information also the information about the displacement the line-of-sight component of the displacement  $\Delta R_d$  enters directly into the interferometric phase as

$$\phi_1 \approx \frac{4\pi}{\lambda} B_{\parallel 1} + \frac{4\pi}{\lambda} \Delta \tau_d = \frac{4\pi}{\lambda} B_1 \sin(\theta_1 - \alpha_1) + \frac{4\pi}{\lambda} \Delta R_d \quad (4.93)$$

To measure the displacement using the interferometric phase of Eq.(4.93), the topography induced phase term should be removed. There are three possible approaches for the removal. The first, and simplest one, is to use a zero-baseline interferometric image pair. In this case, no topography is measured and the phase variation in the interferogram is related only to the height deformations due to the displacement. Consequently, the line-of-sight component of the displacement can be measured directly by means of Eq.(4.93). Unfortunately, the state-of-the-art in navigation today allows the acquisition of zero-baseline interferograms only by accident. The second possible way is to use an available elevation model to generate a simulated interferogram as it will appear under the imaging geometry of the real interferogram [87],[85]. This interferogram now, is used to remove the flat-earth and the topographic phase terms. The limitation of that approach is, apart from the availability, the precision of the reference elevation model. The height errors have to be smaller than the displacement itself. In view of displacements of the order of centimeters this is a hard, if not an unattainable, requirement for any conventional elevation model.

In the following, we will focus on a third, purely interferometric, possibility to remove the topography using a third SAR image of the scene. Assuming this third image to be acquired before the deformation process, the received signal from the point P is

$$s_3(R_3) = |s_3(R_3)| \exp\left(\frac{4\pi}{\lambda} R_3\right) \quad (4.94)$$

and the interferometric phase of an interferogram, formed between the first and the third image, will contain only the original topography

$$\phi_2 \approx \frac{4\pi}{\lambda} B_{2\parallel} = \frac{4\pi}{\lambda} B_2 \sin(\theta_2 - \alpha_2) \quad (4.95)$$

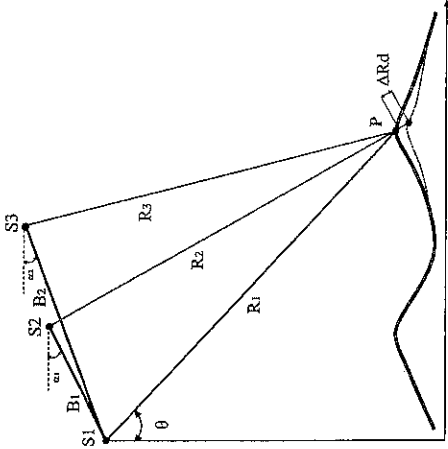


Figure 4.7: Geometry of differential interferometry.

Rescaling the phase of the first interferogram by the ratio of the parallel baseline components

$$\frac{B_{\parallel 12}}{B_{\parallel 1}} \phi_1 = \frac{4\pi}{\lambda} B_{\parallel 2} \quad (4.96)$$

and subtracting it from the first interferogram by means of forming a differential interferogram, we obtain the phase term caused only by the line-of-sight component of the displacement  $\Delta R_d$

$$\phi_d = \phi_2 - \frac{B_{\parallel 2}}{B_{\parallel 1}} \phi_1 = \phi_2 - \frac{B_2 \sin(\theta_1 - \alpha)}{B_1 \sin(\theta_2 - \alpha)} \phi_1 = + \frac{4\pi}{\lambda} \Delta R_d \quad (4.97)$$

One note of caution is required for evaluating Eq.(4.97): the ratio  $B_{\parallel 2}/B_{\parallel 1}$  depends on the look angle  $\theta$ , which is composed by a reference look angle  $\theta_0$  and the a local look angle  $\Delta\theta_z$  (see Section 4.8). While  $\theta_0$  is known for a given imaging geometry,  $\Delta\theta_z$  depends on the local topography. This worrying dependence on the topography can be widely removed by subtracting the flat-earth component from both interferograms

$$\phi_{f_1} = \frac{4\pi}{\lambda} B_1 [\sin(\theta_{01} + \Delta\theta_z - \alpha_1) - \sin(\theta_{01} - \alpha_1)] + \frac{4\pi}{\lambda} \Delta R_d \quad (4.98)$$

$$= \frac{4\pi}{\lambda} B \sin(\theta_{01} - \alpha_1) \Delta\theta_z + \frac{4\pi}{\lambda} \Delta R_d$$

$$\phi_{f_2} = \frac{4\pi}{\lambda} B_2 [\sin(\theta_{02} + \Delta\theta_z - \alpha_2) - \sin(\theta_{02} - \alpha_2)]$$

$$= \frac{4\pi}{\lambda} B \sin(\theta_{02} - \alpha_2) \Delta\theta_z \quad (4.99)$$

where we assumed  $\Delta\theta_{z1} \approx \Delta\theta_{z2}$ . The remaining steps are straightforward. Rescaling  $\phi_{f_2}$  by the ratio of the orthogonal baseline components, which is independent now of the local topography,

we obtain the wanted phase term  $\phi_d$  as

$$\phi_d = \phi_{f_1} - \frac{B_{11}}{B_{12}} \phi_{f_2} = \phi_{f_1} - \frac{B \sin(\theta_{0_1} - \alpha)}{B \sin(\theta_{0_2} - \alpha)} \phi_{f_2} = \frac{4\pi}{\lambda} \Delta R_d \quad (4.100)$$

There is one last remaining point in the determination of  $\phi_d$ . Both interferometric phases are measured only to modulo  $2\pi$ . The phase discontinuities in the two interferograms will not occur at the same places, and thus, at the least one of the interferometric phases has to be unwrapped before performing the subtraction of Eq.(4.100). Nevertheless, Eq.(4.100) addresses an extraordinarily sensitive way of measuring elevation changes. The height sensitivity of the differential interferogram is given by

$$\frac{\Delta\phi_d}{\Delta R_d} = -\frac{4\pi}{\lambda} \quad (4.101)$$

Assuming a sensor operating at L-band with a phase resolution of  $3^\circ$ , the theoretical displacement resolution is in the order of  $1 \text{ mm}$ !!! Thus, while radar interferometry measures topography to an accuracy in the order of meters, displacements may be determined in the order of centimeters or millimeters even from a satellite operating at a range of some hundreds of kilometers. This is a direct consequence of the fact that displacements appears unscaled into the interferometric phase, while the topography is scaled by the baseline geometry (see Eq.(4.93)). The key of that approach, apart of the required high scene coherence among the three observations, which is more critical because of the needed phase unwrapping step, is the accurate knowledge of the interferometric imaging geometry. It is obvious that errors in the knowledge of the baseline parameters could leave residual phase variations which are not distinguishable from differential displacements.

Further, it is evident that the temporal coherence is a serious limitation for differential SAR interferometry. If the relative positions of the effective scattering centers within a resolution cell are changed by the deformation process, the loss of interferometric coherence avoids the extraction of any useful information from the interferogram. On the other hand, macroscopic coherent deformations of the scene, which do not affect significantly the effective scattering centers within the resolution cells, provides sufficient temporal stability for the application of differential interferometry.

## 5 Polarimetric SAR Interferometry

### 5.1 Vector Interferometry

Up to now, radar polarimetry and interferometry were considered as two separate topics. We were concerned either with the case of a fully polarimetric radar system acquiring one single polarimetric vector image (in form of a  $2 \times 2$  complex scattering matrix  $[S]$ ), or with the case of a single-polarisation interferometric system acquiring, from spatially separated locations, two scalar images. This Chapter 5 is concerned with the effects of polarisation on SAR interferometry based on the analysis of data acquired in a interferometric mode using a fully-polarimetric system.

In this first section, we work out the theoretical framework of vector interferometry, which has to include conventional scalar interferometry as a special case. For this, we need to reformulate scalar interferometry in a way different from that described in Chapter 4. The generation of scalar interferograms can be described as the formation of the average hermitian product of the two complex scalar signals,  $s_1$  and  $s_2$ , for the same resolution element received from two spatially separated antennas. Of special significance in this context is the  $2 \times 2$  hermitian positive semi-definite coherency matrix  $[J]$  which we define as

$$[J] := \begin{bmatrix} J_{11} & J_{12} \\ J_{21} & J_{22} \end{bmatrix} = \left\langle \begin{bmatrix} s_1 \\ s_2 \end{bmatrix} \begin{bmatrix} s_1^* & s_2^* \end{bmatrix} \right\rangle = \begin{bmatrix} \langle s_1 s_1^* \rangle & \langle s_1 s_2^* \rangle \\ \langle s_2 s_1^* \rangle & \langle s_2 s_2^* \rangle \end{bmatrix} \quad (5.1)$$

From  $[J]$  we obtain an expression for the phase of the interferogram  $\phi = \arg\{s_1 s_2^*\}$  as

$$\phi = \arctan \left( \frac{\text{Im}\{s_1 s_2^*\}}{\text{Re}\{s_1 s_2^*\}} \right) + 2\pi N \quad \text{with} \quad N = 0, \pm 1, \pm 2, \dots \quad (5.2)$$

The phase  $\phi$  contains both range and topography dependent information. The interferometric coherence  $\gamma$ , defined as the absolute value of the normalised complex cross-correlation between both signals, may be written in terms of the elements of  $[J]$  as

$$\gamma = \frac{|\langle s_1 s_2^* \rangle|}{\sqrt{\langle s_1 s_1^* \rangle \langle s_2 s_2^* \rangle}} = \frac{|J_{12}|}{\sqrt{J_{11} J_{22}}} \quad \text{where} \quad 0 \leq \gamma \leq 1 \quad (5.3)$$

Eqs.(5.1-3) address the case of conventional interferometry in the two-dimensional complex space in terms of the elements of the matrix  $[J]$ .

A monostatic, fully-polarimetric interferometric system measures for each resolution element in the scene, from two slightly different look angles, two scattering matrices,  $[S_1]$  and  $[S_2]$ .